Charge imbalance in superconductors in the low-temperature limit

F. Hübler,[1,2,3] J. Camirand Lemyre,[1] D. Beckmann,[1,2,*] and H. v. Löhneysen[2,3,4]
[1]*Institut für Nanotechnologie, Karlsruher Institut für Technologie, Karlsruhe, Germany*
[2]*Center for Functional Nanostructures, Karlsruher Institut für Technologie, Karlsruhe, Germany*
[3]*Institut für Festkörperphysik, Karlsruher Institut für Technologie, Karlsruhe, Germany*
[4]*Physikalisches Institut, Karlsruher Institut für Technologie, Karlsruhe, Germany*
(Received 5 February 2010; revised manuscript received 19 April 2010; published 21 May 2010)

We explore charge imbalance in mesoscopic normal-metal/superconductor multiterminal structures at very low temperatures. The investigated samples, fabricated by e-beam lithography and shadow evaporation, consist of a superconducting aluminum bar with several copper wires forming tunnel contacts at different distances from each other. We have measured in detail the local and nonlocal conductance of these structures as a function of the applied bias voltage V, the applied magnetic field B, the temperature T, and the contact distance d. From these data the charge-imbalance relaxation length λ_{Q^*} is derived. The bias-resolved measurements show a transition from dominant elastic scattering close to the energy gap to an inelastic two-stage relaxation at higher bias. We observe a strong suppression of charge imbalance with magnetic field, which can be directly linked to the pair-breaking parameter. In contrast, practically no temperature dependence of the charge-imbalance signal was observed below 0.5 K. These results are relevant for the investigation of other nonlocal effects such as crossed Andreev reflection and spin diffusion.

DOI: 10.1103/PhysRevB.81.184524 PACS number(s): 74.40.Gh, 74.25.F−

I. INTRODUCTION

Nonequilibrium phenomena in superconductors have been investigated intensively since the 1970s. Both experimental and theoretical investigations of charge imbalance have focused mostly on temperatures near the critical temperature T_c of the superconductor. In this regime, charge imbalance is easily accessible to experiments basically due to the divergence of the signal toward T_c and excellent theoretical approximations are available.[1–3] Recently, the investigation of nonlocal transport properties of superconductors has gained new impetus from two separate but loosely related fields. One is the investigation of spin-dependent transport,[4] and in particular spin diffusion and accumulation in the context of spintronics. The second is the investigation of coherent nonlocal effects such as crossed Andreev reflection,[5] which might be useful for quantum-information processing. In the diffusive quasi-one-dimensional structures typically used for such experiments, the magnitude of the signals due to these phenomena scale with the normal-state resistance of the superconductor over a characteristic length scale, which is given by the charge-imbalance relaxation length $\lambda_{Q^*} \sim 10\ \mu\text{m}$,[3] the spin-diffusion length $\lambda_{sf} \sim 1\ \mu\text{m}$,[6,7] and the coherence length $\xi \sim 0.1\ \mu\text{m}$,[8] respectively. Consequently, the signals due to charge imbalance are often the largest and make an unambiguous identification of the other phenomena difficult. In particular, for the investigation of crossed Andreev reflection, experiments far below T_c are necessary. Despite the vast amount of experimental and theoretical literature on charge imbalance, surprisingly little is known about the subject at very low temperatures.[9] This is probably due to the fact that no simple theoretical models are available for this regime and that the interpretation of the widely used nonlocal resistance measurement scheme becomes increasingly difficult as temperature is lowered.

In this paper, we report on a detailed investigation of nonlocal *conductance* rather than *resistance* in superconductor/normal-metal hybrid structures at temperatures $T \ll T_c$. The samples consist of a quasi-one-dimensional superconducting wire with several normal-metal tunnel junctions attached to it. From these experiments, we deduce the charge-imbalance relaxation length λ_{Q^*} as a function of bias voltage, temperature, and magnetic field. The results allow a detailed comparison to theoretical predictions for different charge-imbalance relaxation mechanisms and an assessment of the possible impact on the interpretation of experiments on crossed Andreev reflection and spin diffusion.

II. THEORY

Charge imbalance (CI) can be described using two different theoretical frameworks, the quasiparticle, or two-fluid, approach,[1,2,10,11] and quasiclassical Green's functions.[12] The relation of these two approaches has been discussed extensively in the literature.[13,14] We simply note here that the Green's function method is more general, and can be applied, e.g., to inhomogeneous superconducting states and situations with strong pair breaking. We will nevertheless use the quasiparticle approach, due to its conceptual (and computational) simplicity, and discuss its shortcomings where necessary.

We consider a quasi-one-dimensional superconductor of length L along the x axis with several normal-metal electrodes attached via tunnel junctions. These electrodes will serve both to inject nonequilibrium quasiparticles into the superconductor and to detect them. The quasiparticle energies E are given by

$$E = \sqrt{\epsilon^2 + \Delta^2}, \tag{1}$$

where ϵ is the normal-state electron energy relative to the Fermi energy and Δ is the pair potential. The normalized quasiparticle density of states is

$$n(E) = \Theta(E-\Delta)\frac{E}{|\epsilon|}, \tag{2}$$

where Θ is the Heaviside function. Charge imbalance is defined as

$$Q^* = 2N_0\int_{-\infty}^{\infty} q(\epsilon)f(\epsilon)d\epsilon, \tag{3}$$

where N_0 is the density of states per spin at the Fermi energy in the normal state, $q(\epsilon)=\epsilon/E$ is the effective quasiparticle charge in units of the elementary charge e, and $f(\epsilon)$ is the quasiparticle distribution function. By using ϵ rather than E as independent variable, we keep track of the electronlike ($\epsilon>0$) and holelike ($\epsilon<0$) branch of the quasiparticle spectrum. In thermal equilibrium, $f(\epsilon)$ is given by the Fermi distribution $f_T(E)$.

It is apparent from Eq. (3) that Q^* is nonzero only if the populations of the electronlike and holelike branches are unequal, i.e., $f(\epsilon)-f(-\epsilon)\neq 0$. Besides this charge-mode (transverse) nonequilibrium, there is also an energy-mode (longitudinal) nonequilibrium characterized by $f(\epsilon)+f(-\epsilon)-2f_T(E)\neq 0$. As will be shown below, the latter enters transport properties only indirectly via the self-consistency equation for the pair potential

$$1+\mathcal{V}\int_{-\infty}^{\infty}\frac{1-2f(\epsilon)}{2\sqrt{\epsilon^2+\Delta^2}}d\epsilon = 0, \tag{4}$$

where $\mathcal{V}$ is the pairing interaction.

The electric current through a tunnel junction between a normal metal held at bias voltage V and a nonequilibrium superconductor is given by the sum of the usual "Giaever" tunnel current $I_T(V)$,[15] and a bias-independent extra current I_{Q^*} due to CI (Ref. 10)

$$I(V) = I_T(V) + I_{Q^*}. \tag{5}$$

Here

$$I_T(V) = \frac{G_N}{e}\int_0^{\infty} n(E)[f_T(E-eV)-f_T(E+eV)]dE, \tag{6}$$

where G_N is the normal-state tunnel conductance and the Fermi functions describe the electron occupation in the normal metal. The excess current is given by

$$I_{Q^*} = -\frac{G_N Q^*}{2eN_0}. \tag{7}$$

As mentioned above, the current I_{Q^*} depends on the nonequilibrium distribution $f(\epsilon)$ only via the charge mode whereas $I_T(V)$ indirectly depends on the energy mode via the gap equation (4).

In the vicinity of the critical temperature T_c of the superconductor, the deviation of the distribution function $f(\epsilon)$ from equilibrium is small and can be approximated by a Fermi function with a shift $\Delta\mu$ of the chemical potential of the quasiparticles relative to the chemical potential of the Cooper pairs.[11] The most convenient measurement technique in this situation is the widely used nonlocal voltage detection scheme, in which the voltage between a normal-metal detector junction and the superconductor is measured. The voltage adjusts such that $I(V_{det})=0$, i.e., the current I_{Q^*} is cancelled by the backflow $I_T(V_{det})$. In the regime where the chemical-potential model applies, this voltage is given by $eV_{det}=\Delta\mu$, i.e., it directly measures the single parameter that characterizes CI. Voltage detection, however, is less useful in the low-temperature regime that we are interested in for two reasons. First, at low temperature the chemical-potential model breaks down and the detector voltage has no longer a simple physical meaning. Second, the nonlinearity and temperature dependence of the tunnel current I_T distort the measured signal. This has already been noted in the earliest experiment on charge imbalance,[1] where the raw data at low temperature had to be corrected by the temperature dependence of the detector junction for comparison with theory. To avoid these shortcomings, we measure the detector current $I_{det}(V_{det}=0)=I_{Q^*}$. Here, the only detector property that enters is the (constant) normal-state conductance and therefore I_{det} is a direct measure of Q^* even for arbitrary nonequilibrium distributions. Experimentally, we measure the differential nonlocal conductance and we will now derive the expression used to evaluate our results.

The distribution function $f(\epsilon)$ is driven out of equilibrium by tunnel injection into a fixed volume Ω of the superconductor at a rate given by[10,16]

$$\frac{\partial f}{\partial t} = \gamma_{tun} = \frac{1}{\tau_{tun}}\left\{\frac{1}{2}\left(1+\frac{\epsilon}{E}\right)[f_T(E-eV)-f(\epsilon)] - \frac{1}{2}\left(1-\frac{\epsilon}{E}\right)[f(\epsilon)-f_T(E+eV)]\right\}, \tag{8}$$

where $\tau_{tun}^{-1}=G_N/2N_0\Omega e^2$. Here, we use the full nonequilibrium distribution $f(\epsilon)$ in the superconductor rather than the thermal distribution used in Ref. 33. However, we retain the assumption that the normal-metal electrode is at thermal equilibrium, described by the shifted Fermi functions $f_T(E\pm eV)$. It is customary to define an injection efficiency $F^*=e\Omega\dot{Q}^*/I$. Since we will be interested in the differential conductance, we use the spectral quantity $f^*(E)=\epsilon^2/E^2$ rather than the usual integral definition. The expression for f^* neglects the nonequilibrium contributions in Eqs. (5) and (8), which are unimportant for an injector junction biased at $|eV|\gtrsim\Delta$. On the other hand, a detector junction held at $V=0$ leads to charge imbalance relaxation at a rate τ_{tun}^{-1} and care must be taken to ensure that this rate is negligible compared to bulk relaxation mechanisms for noninvasive detection.[17] Once injected, nonequilibrium quasiparticles diffuse along the wire with an energy-dependent diffusion constant $D(E)=v_g D_N$,[14,18] where D_N is the normal-state diffusion constant, and $v_g=|\epsilon|/E$ is the normalized group velocity of quasiparticles. Concomitantly, the nonequilibrium distribution relaxes due to different mechanisms, including inelastic electron-phonon scattering,[2,10,19] elastic impurity scattering in the presence of gap anisotropy,[10,16] and magnetic pair breaking.[12,20,21] Charge-imbalance relaxes over a characteristic time $\tau_{Q^*}=Q^*/\dot{Q}^*$, which we will also assume to be energy-dependent, leading to an exponential relaxation on the length scale $\lambda_{Q^*}=\sqrt{D\tau_{Q^*}}$. The steady-state distribution is

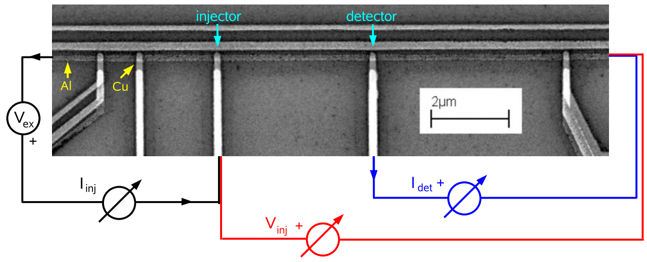

FIG. 1. (Color online) Scanning electron microscopy image of sample A illustrating the experimental scheme. Five copper (Cu) fingers are connected by tunnel contacts to an aluminum bar (Al). For one of the possible injector-detector pairs the bias and measurement scheme used for charge imbalance detection is shown.

achieved when injection and relaxation rates are equal. Assuming that the effective injection volume is given by a wire section of length $2\lambda_{Q^*}$, we find that the nonlocal conductance due to charge imbalance is given by

$$g_{\mathrm{nl}} = \frac{dI_{\mathrm{det}}}{dV_{\mathrm{inj}}} = g^* G_{\mathrm{inj}} G_{\mathrm{det}} \frac{\rho_{\mathrm{N}} \lambda_{Q^*}}{2A} \exp\left(-\frac{d}{\lambda_{Q^*}}\right), \tag{9}$$

where G_{inj} and G_{det} are the normal-state conductances of the injector and detector junctions, ρ_{N} is the normal-state resistivity of the superconductor, and A is the cross section of the wire. The factor g^* accounts for thermal smearing, injection efficiency, etc., and is of order unity. At $T=0$, and neglecting energy relaxation, $g^*=n(E)f^*/v_{\mathrm{g}}=\Theta(eV_{\mathrm{inj}}-\Delta)$. Equation (9) will form the basis for our data analysis.

III. EXPERIMENT

Figure 1 shows the relevant part of one of the three samples discussed, together with a scheme of the measurement setup. All samples are fabricated by e-beam lithography and shadow evaporation techniques. In the following, the processing details are explained with the help of the sample parameters listed in Table I.

First, a copper film with thickness $t_{\mathrm{Cu1}}=25-30$ nm is evaporated onto a thermally oxidized silicon substrate. This first layer will form Ohmic interconnections to the subsequent layers. In the second evaporation step, the superconductor, an aluminum bar of thickness t_{Al} and width w_{Al}, is deposited under a different angle, shifting the design to create intended overlaps only. In order to provide the formation of an insulating layer on the top, the aluminum is then oxidized *in situ* by applying the equivalent of 1 Pa of oxygen for 10 min. In the final evaporation step, a second layer of copper ($t_{\mathrm{Cu2}}=30$ nm) is deposited under a third angle forming five tunnel contacts with the aluminum. The contact distances between neighboring copper fingers presented in sample A are about 1 μm, 2 μm, 4 μm, and 5 μm from left to right, respectively.

For the transport experiment the samples are mounted into a shielded box thermally anchored to the mixing chamber of a dilution refrigerator. The measurement lines are fed through a series of filters to eliminate rf and microwave radiation from the shielded box. A voltage V_{ex} consisting of a dc bias and a low-frequency ac excitation (typically 5 μV at 138 Hz) is applied to the injector contact and the ac part of the resulting current I_{inj} is measured with a lock-in technique. Simultaneously, the ac current I_{det} is measured through the second contact, the detector. The local and nonlocal differential conductances $g_{\mathrm{inj}}=dI_{\mathrm{inj}}/dV_{\mathrm{inj}}$ and $g_{\mathrm{nl}}=dI_{\mathrm{det}}/dV_{\mathrm{inj}}$ are extracted from the ac signals. Voltage and current polarities are indicated in Fig. 1 by plus signs and arrows, respectively. All contacts are measured in a three-point configuration with a series resistance of about 90 Ω coming from the measurement line.

IV. RESULTS

A. Contact and film characterization

To characterize the tunnel contacts and the properties of the superconducting film, we first discuss the tunnel spectra of the individual junctions. Figure 2 shows the local differential conductance g_{inj} as a function of bias V_{inj} for one of the tunnel junctions of sample B. Panel (a) represents the temperature dependence at zero magnetic field whereas panel (b) depicts the variation with magnetic field applied in the plane of the substrate along the Cu wires for constant temperature $T=50$ mK. At lowest temperature and zero field, the differential conductance is completely suppressed at low bias with sharp peaks at the energy gap, showing the high quality of the oxide tunnel barrier. Upon increasing the temperature or the magnetic field, the features are broadened and the gap is reduced. Since we are particularly interested in the dependence on magnetic field, we have used a slightly more elaborate model than Eq. (6) to fit the data. In the presence of a magnetic field, the spin-resolved density of states in the superconductor can be described by[22]

TABLE I. Characteristic parameters of the three samples A–C. Aluminum film thickness t_{Al}, width w_{Al}, and normal-state resistivity ρ_{Al} at $T=4.2$ K, range of contact distances d and contact conductances G, critical temperature T_{c}, critical field B_{c}, and energy gap Δ_0.

	t_{Al} (nm)	w_{Al} (nm)	ρ_{Al} ($\mu\Omega$ cm)	d (μm)	G (μS)	T_{c} (K)	B_{c} (T)	Δ_0 (μeV)
A	30	140	4.9	1–12	230–270	1.39	0.53	208
B	30	190	4.9	0.2–9.7	260–350	1.38	0.58	218
C	12.5	140	11.1	0.5–6.5	370–490	1.5	1.73	225

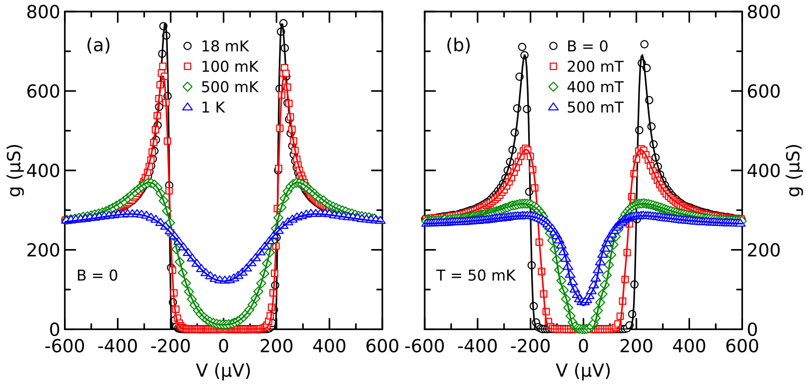

FIG. 2. (Color online) Local differential conductance $g=dI/dV$ of one contact of sample B as a function of bias voltage V for (a) different temperatures T and (b) different applied magnetic fields B. Symbols represent measured data, lines are fits to the model described in the text.

$$n_{\pm}(E)=\frac{1}{2}\mathrm{Re}\left(\frac{u_{\pm}}{\sqrt{u_{\pm}^2-1}}\right), \tag{10}$$

where the complex quantities $u_{\pm}$ have to be determined from the implicit equation

$$\frac{E\mp\mu_B B}{\Delta}=u_{\pm}\left(1-\frac{\Gamma}{\Delta}\frac{1}{\sqrt{1-u_{\pm}^2}}\right)+b_{so}\left(\frac{u_{\pm}-u_{\mp}}{\sqrt{1-u_{\mp}^2}}\right).$$

Here, μ_B is the Bohr magneton, Γ is the pair-breaking parameter, $b_{so}=\hbar/3\tau_{so}\Delta$ measures the spin-orbit scattering strength, and we have dropped a small higher-order term. The fits in Fig. 2 were obtained by replacing the BCS density of states $n(E)$ by $n_+(E)+n_-(E)$ in Eq. (6). During fitting, T and B were taken from the experiment, and the remaining parameters (Δ, Γ, and G_N) were varied. Including the Zeeman splitting was found to be necessary for the data at higher fields. The small spin-orbit term gave minor improvements of the fits but could not be determined precisely. We simply chose a suitable value $b_{so}\sim O(0.01)$ at high field and kept it fixed for all other fits. Similar values can be found in the literature.[23] The quality of the fits was excellent for samples A and B, as shown for the latter in Fig. 2. The pair potential Δ_0 obtained from the fits at lowest temperature and zero magnetic field is listed in Table I. For the thin-film sample C, the quality of the fits was rather poor and no reliable parameters could be obtained. In this case, Δ_0 was determined from the peak position.

For samples A and B, where the fits were reliable, we show the pair-breaking parameter Γ as well as the pair potential Δ as a function of the magnetic field in Fig. 3. In panel (a), the normalized pair potential Δ/Δ_0 is displayed as a function of B/B_c, together with the expectation $\ln(\Delta/\Delta_0)=-(\pi/4)(\Gamma/\Delta)$.[24] The critical pair-breaking strength for the suppression of superconductivity is given by $2\Gamma=\Delta_0$,[24] and together with $\Gamma\propto B^2$ for a thin film in parallel magnetic field,[25] we can rewrite Γ as

$$\frac{\Gamma}{\Delta_0}=\frac{1}{2}\left(\frac{B}{B_c}\right)^2. \tag{11}$$

Figure 3(b) shows Γ/Δ_0 as a function of $(B/B_c)^2$. The solid line is the theoretical expectation in Eq. (11). As can be seen, samples A and B can be described perfectly well by standard pair-breaking theory and we will assume Eq. (11) to hold also for sample C later on.

B. Energy-mode nonequilibrium

While we are mostly interested in charge imbalance, we have also investigated the impact of energy-mode nonequilibrium in our samples. To this effect, we monitor the differential conductance g_{det} of a detector junction while nonequilibrium quasiparticles are injected through a second nearby injector contact. Figure 4(a) shows the differential conductance g_{det} of the left-most contact of sample A (see Fig. 1) as a function of the local bias voltage V_{det} for different injector bias V_{inj} applied to the neighboring contact at a distance of 1 μm. We focus here only on the bias region of the gap features. As the injector bias is increased, the density-of-states peak in the conductance shifts to lower bias and broadens slightly. The increased broadening of the gap features might signify an increased temperature of the normal-metal

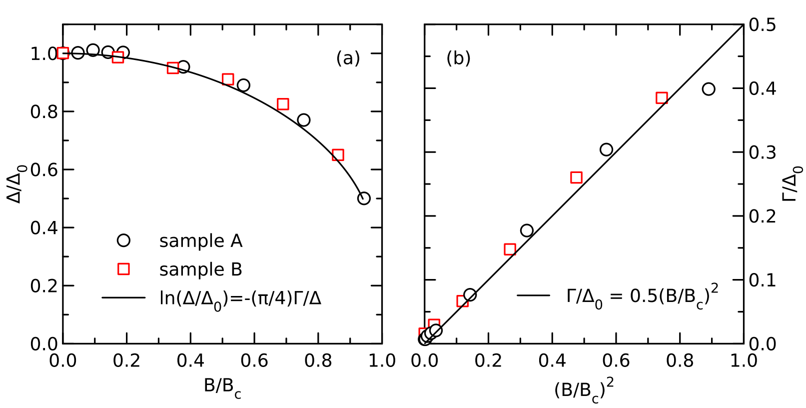

FIG. 3. (Color online) (a) Pair potential Δ as a function of the applied magnetic field B. Δ is normalized to its zero-field value Δ_0 and B is normalized to the critical field B_c. (b) Normalized pair-breaking parameter Γ/Δ_0 as a function of $(B/B_c)^2$. The lines are predictions from pair-breaking theory.

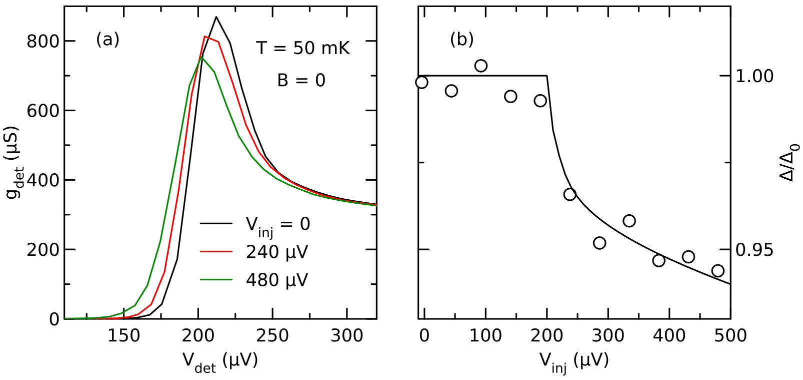

FIG. 4. (Color online) (a) Differential conductance g_{det} of the left-most contact of sample A as a function of bias voltage V_{det} with additional voltage bias V_{inj} applied to the neighbor contact at 1 μm distance. (b) Normalized pair potential Δ/Δ_0 as a function of injector bias V_{inj}. The line is a guide to the eye.

side of the junction due to the injection of nonequilibrium quasiparticles tunneling out of the superconductor.[26] An alternative explanation would be an increased lifetime broadening of the density of states of the superconductor due to scattering of nonequilibrium quasiparticles. From our data, we cannot make a clear decision between these scenarios.

The evolution of the pair potential Δ as a function of injector bias is plotted in panel (b), normalized to its value Δ_0 at $V_{inj}=0$. No significant change is observed for $eV_{inj} < \Delta_0$. As soon as eV_{inj} exceeds $\Delta_0 \approx 200$ μeV, the energy gap drops quickly by a few percent, and continues to decrease more slowly for higher bias. The gap reduction can be understood from the inspection of the self-consistency equation (4). For injector voltages in the vicinity of Δ, a large number of quasiparticles are injected due to the divergence of the density of states. In addition, these quasiparticles are very efficient in reducing the gap due to the energy denominator in the integral. Therefore, the initial decrease is steep, and then becomes more shallow as the density of states flattens, and the denominator increases.

C. Charge-mode nonequilibrium

Figure 5 displays the nonlocal conductance g_{nl} as a function of the injector bias V_{inj} for one injector/detector pair of sample A. Panel (a) shows data for different temperatures T without an applied magnetic field. At $T=50$ mK, the nonlocal conductance is zero within the experimental resolution for bias voltages below $\Delta/e \approx 200$ μV. Above the energy gap, the signal increases continuously from zero with a finite initial slope up to a broad maximum at $V_{inj} \approx 450$ μV before it decreases slowly again. With increasing temperature, the signal smears out around the gap whereas the value at high bias remains unchanged. Panel (b) shows the impact of a magnetic field B applied in the substrate plane along the direction of the copper wires. In contrast to temperature, the signal depends strongly on the magnetic field. The initial slope decreases, and the maximum decreases and shifts to higher bias until it is no longer observable within our bias range for $B \gtrsim 100$ mT.

Figure 6(a) shows the nonlocal differential conductance for several injector/detector contact pairs of sample A at $T=50$ mK and $B=0$. Since $g_{nl} \propto G_{inj} G_{det}$, we have normalized the data accordingly to exclude the impact of small variations in the junction conductances. The overall signal magnitude decreases with increasing contact distance while the shape remains unchanged. Panel (b) shows the normalized nonlocal conductance as a function of contact distance d for different injector bias on a semilogarithmic scale. The solid lines are fits to the exponential decay predicted by Eq. (9). The quality of the fits is generally good, except for the very small signals at lowest bias. From the fits, the relaxation length λ_{Q^*} and the amplitude

$$a = g^* \frac{\rho_N \lambda_{Q^*}}{2A} \tag{12}$$

can be extracted.

The charge imbalance relaxation length λ_{Q^*} extracted from these fits is shown in Fig. 7 as a function of injector bias for different (a) temperatures T and (b) magnetic fields B. The data resemble those of the nonlocal conductance shown in Fig. 5. This is not surprising, since the signal amplitude a is itself proportional to λ_{Q^*}. A noticeable difference

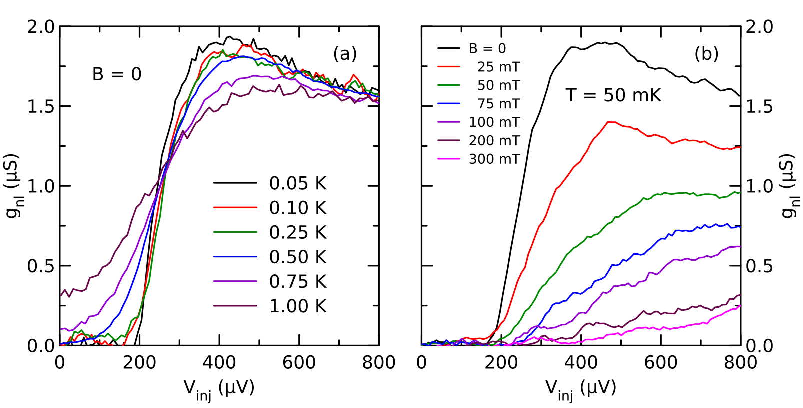

FIG. 5. (Color online) Nonlocal differential conductance $g_{nl}=dI_{det}/dV_{inj}$ for an injector/detector pair of sample A as a function of bias voltage V_{inj} (a) for different temperatures T and (b) for different applied magnetic fields B.

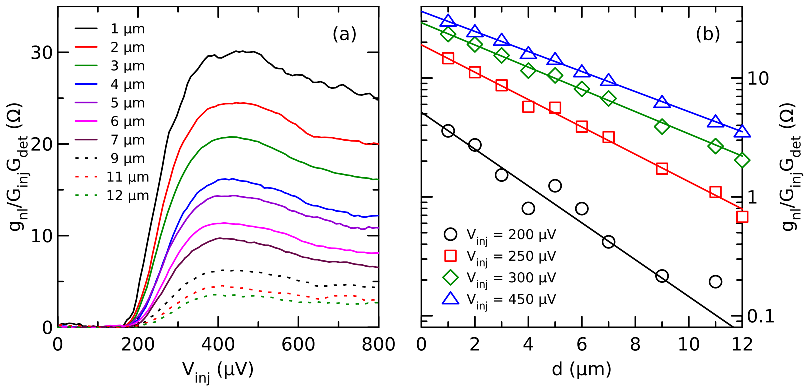

FIG. 6. (Color online) (a) Normalized nonlocal differential conductance $g_{\mathrm{nl}}/G_{\mathrm{inj}}G_{\mathrm{det}}$ as a function of injector bias voltage V_{inj} for different contact distances d. (b) Semilogarithmic plot of $g_{\mathrm{nl}}/G_{\mathrm{inj}}G_{\mathrm{det}}$ as a function of contact distance d for different injector bias V_{inj}. The solid lines are fits to Eq. (9).

is that λ_{Q^*} is nearly independent of temperature. This indicates that the temperature dependence seen in Fig. 5(a) is mostly due to thermal broadening of the distribution in the injector contact rather than a change in relaxation rates. In contrast, the suppression of the nonlocal conductance upon increasing the magnetic field is reflected in the pronounced field dependence of λ_{Q^*}, indicating an increase in the relaxation rate.

Similar results to those presented in Figs. 5–7 were obtained for all three samples. From λ_{Q^*}, we can calculate $\tau_{Q^*}=\lambda_{Q^*}^2/D_{\mathrm{N}}v_{\mathrm{g}}$. The maximum values of λ_{Q^*} and τ_{Q^*} obtained at lowest temperature and zero magnetic field are listed in Table II along with the maximum of the ratio $\tau_{Q^*}/\tau_{\mathrm{tun}}$. We find $\tau_{Q^*}/\tau_{\mathrm{tun}}\ll 1$ for all samples, confirming that our detector junctions are noninvasive.

We will now focus in more detail on the suppression of charge imbalance as a function of magnetic field. Figure 8(a) shows the normalized charge-imbalance relaxation rate $\hbar/\Delta_0\tau_{Q^*}$ as a function of the normalized pair-breaking parameter Γ/Δ_0 for fixed injector bias. Here we have made use of Eq. (11) to calculate Γ from B for all three samples. The data from all samples fall onto a single line and the relaxation rate at zero field is negligible on the scale of the plot. We note that in the magnetic-field range of the plot ($B\lesssim 0.5B_{\mathrm{c}}$) the spectral properties of the superconductor remain almost unchanged. The reduction in Δ, for example, is less than 10% in this range. The relaxation rate due to elastic pair-breaking perturbations such as magnetic impurities,[12,20,27] supercurrent,[21] and applied magnetic field[28] has been calculated both within the quasiparticle description used by us and from quasiclassical Green's functions. We note that by convention, rates from the Green's function formalism differ from those of the quasiparticle description by the factor f^*.[13] When properly adjusted, the rate is predicted to be

$$\frac{1}{\tau_{Q^*}}=\alpha\frac{\Gamma}{\hbar}\frac{\Delta^2}{E\epsilon}, \tag{13}$$

where α is a numerical prefactor of order unity which we will use as a fit parameter. From linear fits of the data in panel (a) we can extract $\hbar/\Gamma\tau_{Q^*}$. The result extracted from such fits is plotted in panel (b) as a function of normalized injector bias $eV_{\mathrm{inj}}/\Delta_0$ for all three samples. The solid line is a joint fit of all data to Eq. (13) (where we have set $E=eV_{\mathrm{inj}}$ and $\Delta=\Delta_0$) with $\alpha=0.73$.

From the signal amplitude a extracted from the fits in Fig. 6, we can calculate the prefactor g^* using Eq. (12) together with known sample parameters and λ_{Q^*} extracted from the same fits. The results are plotted in Fig. 9 as a function of normalized injector bias (a) for all samples at $B=0$ and (b) for sample A at different magnetic fields. At $B=0$, g^* follows the expectation $g^*\approx\Theta(eV_{\mathrm{inj}}-\Delta)$ for samples A and B, whereas it deviates at low bias both for sample C, and in the presence of a magnetic field. Since g^* depends on a combination of several spectral properties of the superconductor, we cannot identify the precise cause of these deviations. For sample C, the enhanced energy-mode nonequilibrium due to the reduced film thickness may play a role. However, in all cases $g^*\approx 1$ at high bias, which justifies our choice of using a wire section of length $2\lambda_{Q^*}$ as injection volume.

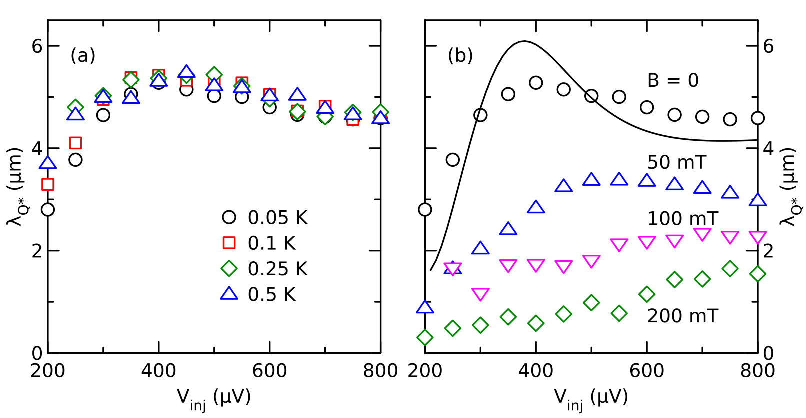

FIG. 7. (Color online) Charge imbalance relaxation length λ_{Q^*} as a function of injector bias voltage V_{inj} for (a) different temperatures T and (b) different applied magnetic fields B. The line is the result of a numerical simulation described in Sec. V.

TABLE II. Maximum values of the relaxation length λ_{Q^*}, the relaxation time τ_{Q^*}, and the ratio $\tau_{Q^*}/\tau_{\mathrm{tun}}$ for all three samples.

Sample	λ_{Q^*} (μm)	τ_{Q^*} (ns)	$\tau_{Q^*}/\tau_{\mathrm{tun}}$
A	5.2	7.8	0.01
B	4.3	5.2	0.01
C	3.0	5.9	0.05

V. DISCUSSION

The bias dependence of the nonlocal conductance can be understood as follows: Charge-imbalance relaxation takes place mostly at energies close to Δ, since the coherence factors for scattering between the electronlike and holelike branches, both elastic and inelastic, vanish at higher energies. In addition, in the low-temperature regime the inelastic contribution is expected to be negligible.[29] The elastic relaxation rate, both due to gap anisotropy and magnetic pair breaking, diverges for $E\rightarrow\Delta$, and quickly drops at higher energies. Consequently, charge imbalance rises continuously from zero as the bias is increased above Δ and in this regime relaxation is mainly due to direct scattering between the branches. As the bias is increased further, the direct relaxation rate decreases. On the other hand, energy relaxation due to inelastic scattering becomes important and charge relaxation turns into a two-stage process.[2] Quasiparticles are first cooled to the vicinity of Δ by inelastic scattering and are then scattered elastically between branches. If we assume that inelastic scattering is described by electron-phonon scattering in the Debye approximation, the inelastic rate quickly increases as more phonons become available at higher energy. Consequently, the nonlocal differential conductance begins to drop again after its initial increase. The bias at which the maximum appears scales roughly with the transition between the direct and two-stage relaxation regimes. The temperature dependence, or lack thereof, can be understood easily from this picture. Elastic relaxation depends only weakly on temperature via Δ. For inelastic relaxation, at low temperatures the Bose factors for emission and absorption of phonons become ≈ 1 and ≈ 0, respectively. Relaxation is then dominated by phonon emission at a rate which only depends on the bias-dependent energy of the quasiparticles but not on temperature. Consequently, the relaxation rate, and λ_{Q^*}, become practically independent of temperature over the entire bias range, as observed in Fig. 7(a). We have identified the quasiparticle energy with the bias voltage throughout our data analysis in Sec. IV. This has to be taken with some caution due to the presence of inelastic energy relaxation. Our approximation mainly affects the calculation of $\tau_{Q^*}=\lambda_{Q^*}^2/D_{\mathrm{N}}v_{\mathrm{g}}$, where v_{g} should actually be an average over energy. However, since inelastic relaxation is important mostly at higher energies, where $v_{\mathrm{g}}\approx 1$, we assume that the error is small. This is corroborated by the observation that the position of the maximum in g_{nl} does not depend much on contact distance, as seen in Fig. 7(a). We would nevertheless like to stress that λ_{Q^*} and τ_{Q^*} are not really spectral quantities but depend in detail on the nonequilibrium distribution and bias conditions.

To make a quantitative connection to microscopic theory, we have performed numerical simulations of the quasiparticle Boltzmann equation, basically following Ref. 32. We have used the one-dimensional form of the Boltzmann equation[14,16]

$$\frac{\partial f}{\partial t} - v_{\mathrm{g}} D_{\mathrm{N}} \frac{\partial^2 f}{\partial x^2} = \gamma_{\mathrm{tun}} - \gamma_{\mathrm{el}} - \gamma_{\mathrm{in}}. \tag{14}$$

The elastic and inelastic relaxation rates γ_{el} and γ_{in} are given by Eqs. (2.16) and (2.17) of Ref. 32, respectively. The injection rate is given by Eq. (8). Steady-state solutions $f(\epsilon,x)$ of the Boltzmann equation (14) were obtained by numerical iteration on a discretized grid. Both injector and detector junctions were included on an equal footing, with injection rates and currents given by Eqs. (5) and (8). Here, the injection volume Ω is given by the grid point size and the spreading of charge imbalance over the length scale λ_{Q^*} is included microscopically in the diffusion term. The granularity of the grid was chosen sufficiently small ($\Delta\epsilon=20$ μeV, $\Delta x=500$ nm) not to affect the results. Parameters such as wire geometry, diffusion constant, contact conductances G_{inj} and G_{det}, etc., were taken directly from the experiment, leaving only the characteristic electron-phonon scattering time τ_0 and the average gap anisotropy $\langle a^2\rangle_0$ as free parameters.

The results of the simulation are shown as a solid line in Fig. 7(b), where we have inserted the typical values $\tau_0=100$ ns and $\langle a^2\rangle_0=0.03$ from Ref. 32. The overall magnitude and shape is predicted correctly by the simulation, with $\lambda_{Q^*}\approx 5$ μm, and a broad maximum at $V_{\mathrm{inj}}\approx 400$ μV. How-

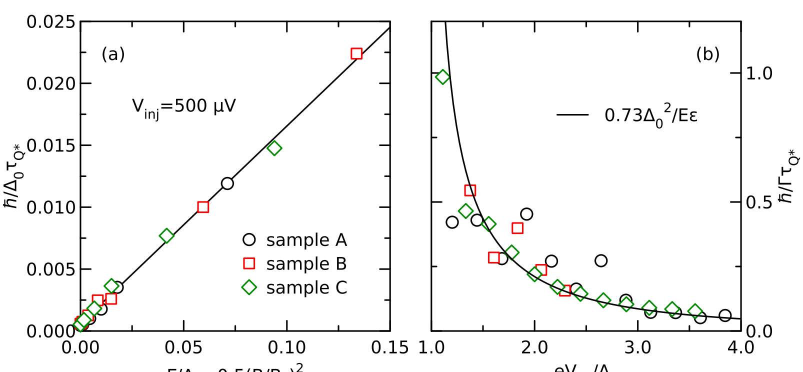

FIG. 8. (Color online) (a) Normalized charge-imbalance relaxation rate $\hbar/\Delta_0\tau_{Q^*}$ as a function of the normalized pair-breaking parameter Γ/Δ_0. The line is a guide to the eye. (b) Normalized charge-imbalance relaxation rate $\hbar/\Gamma\tau_{Q^*}$ as a function of normalized injector bias $eV_{\mathrm{inj}}/\Delta_0$. The line is a joint fit to the data of all three samples.

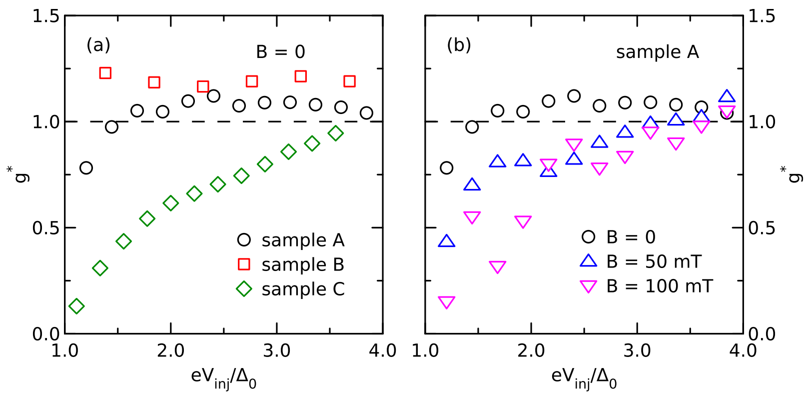

FIG. 9. (Color online) g^* as a function of normalized injector bias $eV_{\mathrm{inj}}/\Delta_0$ (a) for all samples at $B=0$ and (b) for sample A at different magnetic fields B.

ever, in detail the agreement is rather poor. The slope is too steep, both below and above the maximum. The relaxation rate due to impurity scattering has been calculated both within the quasiparticle approach[10,16] and using quasiclassical Green's functions.[29] In contrast to the quasiparticle approach, the Green's function approach predicts different energy dependences for the clean and dirty limits. This difference might explain the discrepancy at low bias. At high bias, electron-phonon scattering in the Debye approximation[19] apparently overestimates the energy dependence of the relaxation rate. A weaker energy dependence has been predicted for electron-phonon scattering in the presence of disorder.[30] It has also been argued that disorder-enhanced electron-electron interaction may dominate, in particular, in aluminum with its weak electron-phonon interaction.[31] Furthermore, neither nonequilibrium distributions on the normal-metal side of the detector junction,[9,26] as suggested by the data in Fig. 4(a), nor spatial variation in the pair potential[32] near the injector junction, as seen in Fig. 4(b), are included in our model. A more detailed simulation based on microscopic theory might provide additional insight into the nonequilibrium conditions and relaxation mechanisms here but this is beyond the scope of this paper.

We now focus on the dependence on magnetic field. Magnetic pair breaking adds an elastic contribution to the relaxation rate.[12,20,21,27,28] Consequently, as B increases, the initial slope of the differential conductance decreases, and the maximum, i.e., the transition to the two-stage relaxation regime, shifts to higher bias. We find that the magnetic contribution to the relaxation rate is directly proportional to the pair-breaking parameter Γ and that its energy dependence follows the theoretical prediction independent of sample details. Our observation $\tau_{Q^*}^{-1} \propto \Gamma$ is markedly different from the well-established approximation $\tau_{Q^*}^{-1} \propto \sqrt{1+2\tau_{\mathrm{E}}\Gamma/\hbar}$ valid for $T \to T_c$,[12] where τ_{E} is the energy relaxation time (note that our $\Gamma/\hbar$ is the magnetic pair-breaking rate, i.e., the quantity τ_s^{-1} of Ref. 28). Magnetic relaxation dominates all other contributions even at very low magnetic fields, where the spectral properties of the superconductor are almost unaffected by pair breaking.

We finally discuss the possible impact of charge imbalance on the observation of other phenomena. We first note that the nonlocal conductance at subgap energies remains negligible at lowest temperatures, even with an applied magnetic field. This is not surprising, since even in the presence of magnetic pair breaking the superconductor still has a well-defined energy gap for quasiparticle excitations, at least as long as pair breaking is not too strong. Also, the relaxation length is always larger than the coherence length ($\xi \approx 100$ nm for our samples). Thus, the dependence of nonlocal conductance on bias or contact distance remains a good criterion to distinguish coherent subgap transport from charge imbalance. On the other hand, the observation of spin-dependent quasiparticle transport necessarily involves injection at energies above the gap and ferromagnetic electrodes must be used. At magnetic fields of ~ 100 mT, which are easily reached by the fringing fields of electrodes made of elementary ferromagnets, λ_{Q^*} can already be as small as 1 μm. This is similar to the spin-diffusion length λ_{sf} in aluminum,[7] and consequently great care must be taken to distinguish charge imbalance and spin-dependent transport.

VI. CONCLUSION

In conclusion, we have presented a detailed investigation of charge imbalance in superconductors in the low-temperature regime. From our measurements, we have extracted the charge-imbalance relaxation length as a function of bias voltage, temperature, and magnetic field. The bias-dependent results allow for a detailed comparison with different relaxation mechanisms. In particular, we have shown a transition from dominant elastic relaxation in the vicinity of the energy gap to an inelastic two-stage relaxation at high bias. The dependence on magnetic field follows theory with remarkable accuracy and is clearly different from the known approximations for the high-temperature regime. The strong reduction in the relaxation length with magnetic field has possible implications for the interpretation of spin-diffusion experiments. During the preparation of this manuscript we became aware of three related studies of charge imbalance at low temperatures.[33]

ACKNOWLEDGMENTS

We thank K. Yu. Arutyunov, W. Belzig, and D. S. Golubev for useful discussions. This work was supported by the DFG Center for Functional Nanostructures and by the DAAD within the RISE program.

*detlef.beckmann@kit.edu

[1] J. Clarke, Phys. Rev. Lett. **28**, 1363 (1972).

[2] M. Tinkham and J. Clarke, Phys. Rev. Lett. **28**, 1366 (1972).

[3] D. N. Langenberg and A. I. Larkin, *Nonequilibrium Superconductivity* (North-Holland, Amsterdam, 1986).

[4] M. Johnson, Appl. Phys. Lett. **65**, 1460 (1994); N. Poli, J. P. Morten, M. Urech, A. Brataas, D. B. Haviland, and V. Korenivski, Phys. Rev. Lett. **100**, 136601 (2008); P. S. Luo, T. Crozes, B. Gilles, S. Rajauria, B. Pannetier, and H. Courtois, Phys. Rev. B **79**, 140508(R) (2009).

[5] J. M. Byers and M. E. Flatté, Phys. Rev. Lett. **74**, 306 (1995); G. Deutscher and D. Feinberg, Appl. Phys. Lett. **76**, 487 (2000); D. Beckmann, H. B. Weber, and H. v. Löhneysen, Phys. Rev. Lett. **93**, 197003 (2004); D. Beckmann and H. v. Löhneysen, Appl. Phys. A: Mater. Sci. Process. **89**, 603 (2007); S. Russo, M. Kroug, T. M. Klapwijk, and A. F. Morpurgo, Phys. Rev. Lett. **95**, 027002 (2005); P. Cadden-Zimansky and V. Chandrasekhar, *ibid.* **97**, 237003 (2006); P. Cadden-Zimansky, Z. Jiang, and V. Chandrasekhar, New J. Phys. **9**, 116 (2007); P. Cadden-Zimansky, J. Wei, and V. Chandrasekhar, Nat. Phys. **5**, 393 (2009); I. Asulin, O. Yuli, G. Koren, and O. Millo, Phys. Rev. B **74**, 092501 (2006); A. Kleine, A. Baumgartner, J. Trbovic, and C. Schönenberger, EPL **87**, 27011 (2009); L. Hofstetter, S. Csonka, J. Nygård, and C. Schönenberger, Nature (London) **461**, 960 (2009); L. G. Herrmann, F. Portier, P. Roche, A. L. Yeyati, T. Kontos, and C. Strunk, Phys. Rev. Lett. **104**, 026801 (2010); J. Brauer, F. Hübler, M. Smetanin, D. Beckmann, and H. v. Löhneysen, Phys. Rev. B **81**, 024515 (2010).

[6] M. Johnson and R. H. Silsbee, Phys. Rev. Lett. **55**, 1790 (1985); T. Valet and A. Fert, Phys. Rev. B **48**, 7099 (1993).

[7] F. J. Jedema, H. B. Heersche, A. T. Filip, J. J. A. Baselmans, and B. J. van Wees, Nature (London) **416**, 713 (2002); F. J. Jedema, M. S. Nijboer, A. T. Filip, and B. J. van Wees, Phys. Rev. B **67**, 085319 (2003).

[8] D. S. Golubev, M. S. Kalenkov, and A. D. Zaikin, Phys. Rev. Lett. **103**, 067006 (2009).

[9] R. Yagi, Phys. Rev. B **73**, 134507 (2006).

[10] M. Tinkham, Phys. Rev. B **6**, 1747 (1972).

[11] C. J. Pethick and H. Smith, Ann. Phys. **119**, 133 (1979).

[12] A. Schmid and G. Schön, J. Low Temp. Phys. **20**, 207 (1975).

[13] J. Clarke, U. Eckern, A. Schmid, G. Schön, and M. Tinkham, Phys. Rev. B **20**, 3933 (1979).

[14] O. Entin-Wohlman and R. Orbach, Ann. Phys. **122**, 64 (1979).

[15] I. Giaever, Phys. Rev. Lett. **5**, 147 (1960).

[16] C. C. Chi and J. Clarke, Phys. Rev. B **19**, 4495 (1979); **21**, 333 (1980).

[17] T. R. Lemberger, Phys. Rev. Lett. **52**, 1029 (1984).

[18] J. N. Ullom, P. A. Fisher, and M. Nahum, Phys. Rev. B **58**, 8225 (1998).

[19] S. B. Kaplan, C. C. Chi, D. N. Langenberg, J. J. Chang, S. Jafarey, and D. J. Scalapino, Phys. Rev. B **14**, 4854 (1976).

[20] T. R. Lemberger and J. Clarke, Phys. Rev. B **23**, 1088 (1981).

[21] T. R. Lemberger and J. Clarke, Phys. Rev. B **23**, 1100 (1981).

[22] K. Maki, Prog. Theor. Phys. **32**, 29 (1964).

[23] R. Meservey, P. M. Tedrow, and R. C. Bruno, Phys. Rev. B **11**, 4224 (1975).

[24] A. A. Abrikosov and L. P. Gor'kov, Zh. Eksp. Teor. Fiz. **39**, 1781 (1960) [Sov. Phys. JETP **12**, 1243 (1961)].

[25] K. Maki, Prog. Theor. Phys. **31**, 731 (1964).

[26] Y. Takane, J. Phys. Soc. Jpn. **76**, 043701 (2007).

[27] S. N. Artemenko, A. F. Volkov, and A. V. Zaitsev, J. Low Temp. Phys. **30**, 487 (1978).

[28] Y. Takane and Y. Nagato, J. Phys. Soc. Jpn. **77**, 093713 (2008).

[29] Y. Takane, J. Phys. Soc. Jpn. **75**, 023706 (2006).

[30] G. Bergmann, Phys. Rev. B **3**, 3797 (1971); A. Schmid, Z. Phys. A **259**, 421 (1973); D. Belitz, Phys. Rev. B **36**, 2513 (1987).

[31] M. Stuivinga, C. L. G. Ham, T. M. Klapwijk, and J. E. Mooij, J. Low Temp. Phys. **53**, 633 (1983); J. Clarke, in *Nonequilibrium Superconductivity*, edited by D. N. Langenberg and A. I. Larkin (North-Holland, Amsterdam, 1986), p. 1.; S.-G. Lee and T. R. Lemberger, Phys. Rev. B **40**, 10831 (1989).

[32] Y. Takane, J. Phys. Soc. Jpn. **78**, 064704 (2009).

[33] K. Tsuboi and R. Yagi, J. Phys. Soc. Jpn. **79**, 013704 (2010); A. Kleine, A. Baumgartner, J. Trbovic, D. Golubev, A. Zaikin, and C. Schönenberger, arXiv:0911.4427 (unpublished); K. Y. Arutyunov (unpublished).